Acoustic Emission Monitoring of Hydraulic Fracturing Using Carbon Dioxide in a Small-scale Field Experiment

Tsuyoshi ISHIDA*[a], Shuich DESAKI[a], Yoshinobu KISHIMOTO[a], Makoto NAOI[a] and Hirokazu FUJII[b].

[a]*Kyoto University, C-Cluster, Katsura Campus of Kyoto University Nishikyo-ku, Kyoto 615-8540, JAPAN*

[b]*LAZOC Inc., 1-5-3, Nishikameari, Katsushika-ku, Tokyo, 124-0002，JAPAN*

* *Tsuyoshi Ishida. Tel.: +81-75-393-8589 E-mail address: ishida.tsuyoshi.87c@st.kyoto-u.ac.jp*

ORCID: Tsuyoshi Ishida (ORCID: 0000-0001-6818-6508)

Makoto Naoi (ORCID: 0000-0001-9488-9266) ※ The other authors do not have ORCID

Keywords: Hydraulic Fracturing; Carbon Dioxide; Acoustic Emission; Focal Mechanism; Geothermal Energy; Shale Gas

Abstract

Carbon capture and storage (CCS) is a promising method for mitigating the greenhouse effect. If we could utilize carbon dioxide (CO_2) for recovery of geothermal energy and shale gas, CCS will be much more eagerly developed and adopted by compensating its cost. We clarified that hydraulic fracturing (HF) using CO_2 tended to induce three-dimensionally sinuous cracks with many secondary branches, which appear to be desirable pathways for energy recovery. However, in a laboratory experiment, it was difficult to evaluate crack extension size and effects of macroscopic pre-existing cracks. Thus, we conducted a HF experiment using CO_2 in a hole 10 m long that was drilled in a hot rock mass, thus satisfying the temperature necessary to form supercritical (SC) CO_2. A bi-wing crack 3.33 m in length was induced along the hole; this crack was significantly larger than the approximately 0.5 m long crack we made with water at another site. The fact that acoustic emission (AE) hypocenters distributed in almost perpendicular to an initial HF crack direction without pressure suggested that CO_2 could easily intrude and enhance AE occurrence along a pre-existing crack. Focal mechanisms using P wave first-motion polarities elucidated that many compression-dominant AE events were recorded; these were never observed in similar HF experiment we conducted using water. The compression-dominant events were probably induced by crack closure due to the degassing of injected CO_2. Even if CO_2 injection induces many AE events, the compressive-dominant events out of them unlikely trigger natural earthquakes because they never create new cracks.

1 Introduction

Carbon capture and storage (CCS) in underground reservoir is a promising and feasible method for mitigating the greenhouse effect by decreasing the amount of carbon dioxide (CO_2) emitted into the air. If we could utilize CO_2 for energy production, CCS will be much more eagerly developed and adopted by compensating its cost. The technology utilized is called carbon capture, utilization, and storage (CCUS), and for examples of applications of CCUS to underground resources, Xie et al.[1] shows the recovery of enhanced geothermal systems (CO_2-EGS), enhanced shale gas (CO_2-ESG), enhanced natural gas (CO_2-EGR), enhanced coalbed methane (CO_2-ECBM), enhanced oil (CO_2-EOR) and others. Among these, for geothermal energy extraction in EGS, Brawn[2] and Pruess[3] stated that CO_2 is superior to water as a working fluid. Regarding exploitation of shale gas in ESG, Kalantari-Dahaghi, [4] Liu et al., [5] Middleton et al.[6] and Godec et al.[7] suggested that it is feasible through numerical simulations, because CO_2 has a higher affinity for shale than methane (CH_4) and CH_4 is desorbed with the absorption of CO_2.[8] For these projects, CO_2 is injected into rocks usually at a depth of more than 1000 m and sometimes more than 3000 m, and the temperature and pressure at these depths cause the CO_2 to reach its supercritical (SC) state. SC-CO_2 has a much lower viscosity (0.01 mPa·s to 0.1 mPa·s) than that of water (1 mPa·s). We clarified that hydraulic fracturing (HF) using SC-CO_2 tends to induce three-dimensionally sinuous cracks with many secondary branches, which appear to be desirable pathways for such projects.[9, 10]

However, in a laboratory experiment, it is difficult to evaluate the crack extending size and effects of pre-existing cracks because the cracks extend to the surfaces of the specimen immediately after breakdown (BD) and a specimen usually does not contain a macroscopic pre-existing crack. Thus, we conducted a HF experiment using CO_2 in a hole 10 m long drilled from the tunnel floor of a hot rock mass, which had a pre-existing crack that satisfied the temperature necessary for SC-CO_2 to form. After we conducted this experiment in 2014, we reported the experimental methods and preliminary results on a relation between temporal change of AE source distribution and a pre-existing crack in the symposium of EUROCK 2017.[11] In the symposium of EUROCK 2018, we analyzed the focal mechanisms of these AE events and showed that many of them show compression-dominant mechanism with shear-dominant mechanism.[12] In this paper, we newly examine a size of HF cracks induced by the SC-CO_2 injection using images obtained by a borehole camera. In addition, we newly examine relations between locations and focal mechanisms of the AE events, to clarify a difference of effect on the focal mechanism between a new crack and a pre-existing crack. Through the new examinations, we concurrently discuss and elucidate remarkable features of HF using CO_2 in comparison to conventional HF using water, and effects of a pre-existing crack on them.

2 Site and Experimental Setup

2.1 Site and Method of CO_2 Injection

As shown in Figure 1, the experimental site was situated in a small railroad tunnel approximately 50 m below the surface of a mountainous area in central Japan. The rock mass around the site consisted of granitic rock formed from the late Miocene to the Pliocene. Although the rock temperature was 165 °C when this tunnel was excavated in 1940, it is now 35 °C due to a cooling effect from air circulating through the tunnel for an extended time. A HF hole (86 mm in diameter) was drilled vertically downward from the tunnel floor, and four acoustic emission (AE) monitoring holes (66 mm in diameter each) were drilled parallel to and at 1 m from the HF hole. To inject CO_2, we drilled a pilot hole 36 mm in diameter at the center of the bottom of the HF hole. We selected the pressurizing section from intact rock at a depth of 7.24 m to 7.40 m, where no visible crack was found, by checking the recovered core of the pilot hole. We sealed the upper section of the pilot hole with two O-rings that were attached to a packer unit and poured cement paste above the O-rings, as shown in the inset of Figure 1b. CO_2 was injected into the pressurizing section under the O-rings.

Figure 2 shows the injection system used in the experiment. To inject CO_2, we used two syringe pumps and alternated between them to achieve continuous injecting during the experiment. We fed CO_2 from a bomb into the syringe-pump cylinders, each of which had a capacity of 500 mL. To fill the cylinders as full as possible, we circulated coolant around them to cool the CO_2 therein and to keep it in the liquid state. In the experiment, the liquid CO_2 was discharged from the cylinder at a constant flow rate of 50 mL/min by controlling the displacement of the syringe. The discharged CO_2 was heated up to approximately 50°C by a heater and was injected into the sealed section of the rock at a temperature of 35°C. As shown in the phase diagram of Figure 3, CO_2 reached a SC state at this temperature under the pressure higher than 7.38 MPa.
The CO_2 was injected into a rock mass saturated with water because the groundwater level was approximately 1 m below the tunnel floor.

2.2 Measurement of AE, Pressure, and Temperature

For AE monitoring, we installed four waterproof lead–zirconate–titanate (PZT) sensors with a resonance frequency of 70 kHz (AE703SW-GAMP-0542; Fuji Ceramics

Corp., Japan) in each of the four AE holes (AE1–4 in Figure 1b). We attached each sensor to an aluminum rod with a pre-amplifier and inserted a thick rubber sheet between the sensor and the rod to block any vibrations transmitted through the rod. After orienting each sensor to face the HF hole, we pressed them onto the walls of the AE holes by applying 1.5 MPa of oil pressure in a small hydraulic jack set behind each sensor. In each AE hole, we installed four sensors over a 2 m long span at intervals of 0.7 m, 0.6 m, and 0.7 m to center the 2 m section at the center depth of the pressurizing section of the HF hole.

The recording of an AE event was triggered when one of the signals from the 16 AE sensors (in total) set in the four holes exceeded 1 V. After the AE signals detected at the sensors were amplified by 40 dB in a pre-amplifier and 30 dB in a main-amplifier, they were processed with a band-pass filter between 20 kHz and 200 kHz and recorded on a hard disk through an analog-to-digital (A/D) converter (PXI-5105; National Instruments Corp., USA). The AE signal of each sensor for each event was digitized into 2048 samples with a 1 μs sampling time. We stopped recording for 10 ms, just after recording an event for 2.048 ms, to prevent the hard disk from recording too much noise caused by "ringing," which was the vibration following a large AE event.

We measured the injection pressure with a transducer (PW-50MPA; Tokyo Sokki Kenkyujo Co., Ltd., Japan) that was set on the injection pipe on the floor just outside of the HF hole. The temperature was measured with a T-type thermocouple glued onto the injection pipe just above the cement paste sealing the pressurized section in the HF hole. The pressure and temperature data were recorded by another A/D converter (PXI-6251; National Instruments Corp., USA) with a sampling time of 0.1 s.

2.3 AE Data Processing for Hypocenter Location

For hypocenter location, we adopted the least square iterative method using P wave arrival time. We measured the P wave velocities between the HF hole and the 16 sensors just before and after the HF by using an emitter (AE703SWR-0840; Fuji Ceramics Corp., Japan) attached to the upper part of the packer unit. After confirming that the difference in P wave velocities before and after the HF was small, the average velocity of 5.4 km/s (standard deviation of 0.4 km/s) was used for the hypocenter locations under the assumption that the rock mass was isotropic and homogeneous.

In the following analysis, we used well-located hypocenters whose accuracy is expected to be within 50 mm by satisfying the following two conditions:[13] (1) The P wave arrival times could be read at six or more sensors set in three or more different AE holes to enclose the hypocenter three-dimensionally; (2) the standard deviation and the maximum of residuals of arrival times were within 10 μs and 20 μs, respectively. Satisfying these conditions, we located the hypocenters of 1249 AE events during the CO_2 injection.

3 Results

3.1 Temporal Changes in Fluid Pressure, Temperature, AE Rate, and Flow Rate

Figure 4 shows the temporal changes in fluid pressure, temperature, AE rate and flow rate with elapsed time, *t*. We took $t = 0$ as the time when the pressure reached breakdown (BD) pressure, which was defined as the peak pressure immediately before the large sudden drop. Here, the AE rate was counted for only well-located events (see Section 2.3).

When we opened the valve of the injection system, the bomb pressure of the CO_2 (approximately 1 MPa) acted on the pressurized section. We injected CO_2 at a constant flow rate of 50 mL/min, with a sudden stop for 30 s (from -15 min 13 s to -14 min 43 s), due to a problem with switching the two syringe pumps. The injected pressure increased with the elapsed time, and BD was induced at 15.62 MPa. Immediately after BD, the injection was stopped. A few minutes after BD, we found that bubbles of CO_2 were gushing out from the water that filled the AE1 and AE3 holes.

Initially, the pressure increased gradually with time, and then it increased steeply at approximately $t = -3$ min (indicated by the thick arrow in Figure 4a). This steep increase started at a pressure close to the critical pressure of 7.38 MPa. At that time, the temperature was approximately 35 °C, which was higher than the critical temperature of 31.1 °C. Thus, the steep increase was most likely caused by the decrease in CO_2 compressibility, due to the phase change from the gaseous state to the SC state (see Figure 3). The temperature decreased to 32.6 °C at BD, probably due to the adiabatic expansion of the CO_2. This likely occurred because of the pressure decrease due to the leakage of SC-CO_2 into the induced cracks, which accompanied the phase change from the SC state to the gaseous state.

There were three terms missing from the AE data, as shown by the thick solid line segments in Figure 4b. The first missing term from 1 to 26 s was due to a problem in the acquisition of AE data with an excess of induced AE events. The second and third terms, from 4 min 38 s to 6 min 12 s and from 20 min 31 s to 21 min 44 s, respectively, were due to replacing a file filled with AE data with a new file in the monitoring unit. The decrease in the located AE event rate of the second and third terms was caused by the missing data.

3.2 AE Source Locations and Crack Observations

Figure 5 shows the locations of the AE hypocenters projected onto the horizontal plane, *XY*, and the two vertical planes, *YZ*, and *ZX*. Figure 6 shows the AE hypocenter distributions on the horizontal plane, *XY*, for the period from 0 (BD) to 1 min 15 s in comparison with those from 1 min 15 s to 30 min 0 s. Figure 6 indicates AE hypocenters distributed along A-direction from the HF hole to the AE1 and AE3 holes for the initial 1 min 15 s from BD. After that, they started to distribute along B-direction almost perpendicular to A-direction from the portion close to AE3 hole. From the vertical distributions on the *YZ* and *ZX* planes in Figure 5, the AE hypocenters distribute on the two nearly vertical planes having the strikes of A- and B-directions.

After we analyzed and discussed the AE source distributions, [11,12] we have newly made close observations of a core overcored around the pressurizing section and images obtained on the wall of the HF hole by a borehole camera, to clarify the cracks induced by the HF.

Figure 7 shows a photo of a core of the 36 mm diameter pilot hole drilled to make the pressurizing section before HF and a hollow core recovered by the 86 mm diameter overcoring around the pressurizing section after HF. We could see a crack almost parallel to the drilling direction, as indicated with a red line on the surface of the core recovered by overcoring. The crack direction was confirmed to face the AE1 hole from the HF hole. Also, on the opposite side of the core, there was a similar crack facing the AE3 hole along the drilling direction. These cracks indicated that the HF induced bi-wing vertical cracks in A-direction. Because we confirmed that there was no pre-existing crack in the pressurizing section by inspecting the pilot hole core before HF and the high BD pressure (15.62 MPa) was recorded, it was most likely that the cracks were newly induced in the intact rock at BD, and they extended for 1 min 15 s from BD along the vertical plane having the strike of A-direction. The direction corresponded to the observation that the injected CO_2 gushed out from the AE1 and AE3 holes.

Figure 8 shows cracks observed on the wall of the HF hole by a borehole camera after HF. From this, we can confirm that two parallel cracks were induced in A-direction in the interval of the pressurizing section, and they extended 3.33 m in length from a depth of 6.15 m to 9.48 m, which resulted in an ellipsoidal crack. The vertical length of the crack extension almost corresponds to the AE hypocenter distribution in *Z*-direction, as shown in Figure 5. On the other hand, the AE hypocenters horizontally distributed along B-direction were almost perpendicular to A-direction from the position of approximately 0.6 m away from the HF hole, although no pressure acted in the pressurizing section for the term from 1 min 15 s to 30 min 0 s, as shown in Figure 4a. From this, we could infer that a vertical crack existed in B-direction before HF, and the AE events were induced with the intrusion of gaseous state CO_2 into it.

3.3 Focal Mechanism from P Wave First-Motion Polarities of AE

We examined the focal mechanisms by using P wave first-motion polarities of the AE. The polarity response of the sensors was checked by dropping a steel ball onto the surface of each AE sensor. We confirmed for each sensor that an upward trace corresponded to a compressive wave, and a downward trace corresponded to a dilatant wave. Figure 9 shows the percentage R (%) of a number of the compression polarities to a total number of the polarities we could read for each AE event along with the elapsed time[12]. This analysis was conducted for AE whose polarities could be read at six or more sensors out of the well-located AE events shown in Figures 5 and 6. The number of AE that satisfied the condition was 161 out of the 1249 well-located hypocenters.

The ratio R approaches 100% for a tensile or explosion source, 50% for a pure shear source, and 0% for a compression or implosion source when good coverage of AE sensors around a source is achieved. In the present study, we labelled AE with $100 \geq R \geq 80$ as tensile-dominated (type T), those with $80 > R > 20$ as shear-dominant (type S), and those with $20 \geq R \geq 0$ as compression-dominant (type C). In Figure 9, there are five events labelled as type T within 30 s after BD, although we can only see three symbols in the figure due to overlapping. However, no event labelled as type T was recorded after this time. Immediately after type T events were recorded, many type S events started to be recorded with type C events. They were recorded even after injection was stopped and the injection pressure completely declined as shown in Figure 4a.

In addition to the temporal change of the ratio R[12], we newly show Figures 10 and 11 to examine relation between location of a source and its ratio R. Figure 10 plots the X, Y, and Z coordinates of the AE hypocenters along with the elapsed times for 30 min after BD, which corresponds to those in Figure. 9. Figure 11 plots their distributions on the horizontal plane, XY, for the period from 0 (BD) to 1 min 15 s in comparison with those from 1 min 15 s to 30 min 0 s. The plotted AE events correspond to those shown in Figures 9 and 10; in other words, there are only 161 events satisfying the condition, out of the 1249 well-located AE hypocenters plotted in Figures 5 and 6. Figures 10 and 11 elucidate that four out of the five type T events occurred near the pressurizing section of the HF hole immediately after BD. Following that, immediately after BD in

Figure 10, the hypocenters of the type S and the C events cluster in the range of -0.5 m to 0.1 m in both the *X* and *Y* coordinates, corresponding to the distribution along A-plane in Figure 11a. The type S and type C events are not only located along A-plane but also B-plane after 1 min 15 s, as shown in Figure 11b.

4 Discussion

4.1 Crack Extension with Injection of SC-CO_2

We injected SC-CO_2 into the pressurizing section after confirming there were no pre-existing cracks in it by inspecting the recovered core. However, a 3.33 m long bi-wing crack that extended vertically along the boring axis was observed on images of the HF hole wall obtained by a borehole camera after HF. The horizontal direction of the crack observed on the outer surface of the hollow core recovered by overcoring after HF was consistent with the direction of the AE1 and AE3 holes where the injected CO_2 gushed out. The crack was most likely induced at BD, from the following reasons; (1) the BD pressure (15.62 MPa) was high, (2) the bi-wing crack extended in the vertical, and (3) horizontal directions of the crack extension correspond to the AE hypocenter distributions just after BD.

In a similar HF field experiment, water was injected into the same size pressurizing section of granite (36 mm in diameter and 160 mm long) in Mizunami Underground Research Laboratory (MIU). New cracks extended 0.4 m vertically and 0.3 m horizontally under a flow rate of 10 mL/min, and they extended to 0.7 m and 0.5 m, respectively, after the flow rate was increased to 30 mL/min.[14] In the present experiment, SC-CO_2 was injected at a flow rate of 50 mL/min. Even considering that the flow rate was greater than that of water, the crack extension of 3.33 m vertical and 2 m horizontal was still notably larger than that of water. The difference could be attributed to the effects of expanding gaseous pressure with the phase change of the CO_2 from SC to gas and the lower viscosity of gaseous state CO_2 than that of liquid water. If so, SC-CO_2 can likely make a larger crack than water even under the same flow rate, when both CO_2 and water are measured in a volume of the liquid state in the cylinder of the syringe pump.

After 1 min 15 s from BD, AE hypocenters started to distribute along B-direction almost perpendicular to A-direction from the position of a 0.6 m distance from the HF hole. Because no pressure acted in the pressurizing section of the HF hole in the term, a pre-existing crack most likely existed in the position along B-direction. If so, this indicated that CO_2 could easily intrude and enhance AE occurrence along a pre-existing crack without pressure.

4.2 Fracturing Mechanism of Type T Events

The type T events occurred near the pressurizing section of the HF hole immediately after BD, and this was consistent with the elastic theory explaining that tensile fracture initiates HF. [15-18] This finding was noteworthy because many researchers have reported that shear events are dominant rather than tensile at BD,[19-22] although some researchers have recently reported existence of tensile dominant events.[23-26] Sasaki et al.[27] performed a laboratory HF experiment in a block of impermeable acrylic resin and reported that all AE events (10 in total) were tensile without exception.

A granitic rock generally has two sets of preferred orientation of microcracks[28, 29]. Most of microcracks preferentially oriented along the "rift plane", and a secondary orientation is known as the "grain plane." The "hardway plane" is defined by the plane perpendicular to both the rift plane and the grain plane. The three planes were named by quarrymen, and they split a granitic rock along the rift plane to sprit it easily. Also, in HF experiments, there is a tendency that crack easily extends along the rift plane[30]. Recently, using this nature of a granitic rock, Yamamoto et al.[31] conducted HF experiments using samples of two types of granite under uniaxial loading, namely those with a rift plane perpendicular to the expected direction of macroscopic fracture propagation and those with a rift plane parallel to it (i.e., along the loading axis). They found tensile events to be dominant when the fracture propagated perpendicular to the rift plane, whereas shear events were dominant when the fracture propagated parallel to the rift plane. These laboratory experiments suggest that tensile events are dominant when a fracture propagates in intact rock. In addition, Rodriguez et al.[32] showed that tensile events are concentrated near the edges of the propagating fracture before BD. Also in our similar field experiment using water in the MIU,[14] type T events were recorded immediately after BD; furthermore, most of the type T events were distributed on the borders of regions where AE events had already occurred. These results suggest that new crack propagation in intact rock is induced by tensile fracturing.

4.3 Fracturing Mechanism of Type S Events

After type T events were recorded, many type S events were recorded with type C events. As mentioned above, many researchers have reported that most of the AE recorded with HF are shear events. Also, in volcanic earthquake swarms, significant parts of seismic events show a shear mechanism, although many events are characterized by magma intrusions or eruptions. To explain this observation, Hill[33] proposed the conceptual model that magma intrudes into the weak planes lying along the direction of the maximum compressive stress as well as among many weak planes prevailing in a volcanic region. The magma intrusion, forming a dike, would accompany some tensile fracturing, whereas shear fracture would form conjugate faults, thereby connecting the tips of dikes.

Even in a laboratory three-bending test, shear events were observed to dominate. Kao et al.[34] conducted a three-point-bend fracture test on a granite specimen measuring 217 mm × 73 mm × 32 mm (span × height × thickness) with a 4 mm notch; the AE events were located, and their focal mechanisms were analyzed. They found that all the AE events were shear dominant due to tortuosity reflecting the local deviation of the crack path by grain-scale heterogeneity, although the macroscopic fractures were tensile. This experiment suggests that macroscopic tensile fracture is a natural consequence of shear events associated with tortuosity, and that the local mechanism, i.e. the mechanism of an AE event, does not necessarily reveal the nature of the macro failure mode. Microscopic observations in our laboratory HF experiments using SC-CO_2 with very low viscosity revealed that HF cracks propagated mainly along the grain boundaries of the constituent minerals, producing many small cracks inclined in the direction of the maximum compressive stress, σ_1, which was the propagating direction of the main crack. Because shear stress acted on a plane inclined in the direction of σ_1, a shear fracture could easily occur on the plane.[10]

In the field experiment presented here, when cracks extended from intact rock around the pressurizing section of the HF hole into inhomogeneous rock that contained various weak discontinuities including pre-existing cracks, many type S events were most likely induced with new crack extension or slippage on crack planes inclined to the direction of the macroscopic crack propagation. If a concept, such as this, regarding crack propagation and the origin of AE was accepted, we could understand the reason why many researchers have reported that shear events are dominant with HF in an actual field operation because rock masses in the field have various geological weak discontinuities. In addition to the mechanism, it is likely that pore pressure increased with HF and its increase also enhanced shear events.

4.4 Fracturing Mechanism of Type C Events

As shown in Figures 9 through 11, many type C events were recorded with type S events. However, we never observed type C events in our similar HF experiment using water in the MIU.[14] Thus, type C events are probably a distinctive feature associated with CO_2 injection.

On the other hand, compressive events are often observed in seismicity in volcanic regions. Shimizu et al.[35] and Foulger et al.[36] suggested that these events were induced by crack closure due to degassing from magma. In addition, Ross et al.[23] expected that compressive events should be induced with the removal of large volumes of steam from a geothermal reservoir, and Martínez-Garzón et al.[37] actually observed compressive events at The Geysers geothermal field, California, USA. Bohnhoff and Zoback[38] observed non-shear-mechanism events with the leakage of injected CO_2 at a depth of 900 m underground. Because the depth was close to that of the hydrostatic pressure at which CO_2 changes from SC to the gaseous state, they reasoned that mass advection of CO_2 caused the non-shear-mechanism events. In a laboratory experiment for hydraulics, Warjito et al.[39] showed that a bubble breaking into smaller bubbles induced acoustic waves, and Kolaini[40] pointed out that the acoustic radiation released by bubble breakage changed with the concentration of salt. Thus, the type C events observed in our present experiment were likely induced by crack closure due to the degassing of injected CO_2, mass advection, or the bursting of bubbles. Although CO_2 injection could induce many type C and S events, at least the type C events out of them unlikely trigger natural earthquakes because the type C events never create new cracks.

5 Conclusions

We conducted a HF experiment using SC-CO_2 in a hole drilled into a granitic hot rock at a depth of 7.24 m to 7.40 m below the tunnel floor. During the experiment, we monitored the AE, pressure, and temperature of injected CO_2. After the experiment, we observed a crack induced by HF on the surface of the core recovered by overcoring as well as on images of the HF hole wall obtained by a borehole camera. From the hypocenter location and the focal mechanism of the monitored AE and the crack observations, we concluded the followings:

1. We found a bi-wing vertical crack 3.33 m long along an HF hole on images of the HF hole wall obtained after HF by a borehole camera. The horizontal direction of the crack observed on the surface of the core (recovered by overcoring after HF) was consistent with the directions from the HF hole to the AE1 and AE3 holes where the injected CO_2 gushed out. Because the BD pressure of 15.62 MPa was sufficiently high and the crack extension in the vertical and horizontal directions corresponded to the AE hypocenter distributions just after BD, the crack was most likely induced at BD.

2. In our similar HF field experiment, we injected water into the same size pressurizing section of granite (36mm in diameter and 160 mm in length) in the MIU, and new cracks extended 0.4 m to 0.7 m vertically and 0.3 m to 0.5 m horizontally. Even considering that the injection flow rate of SC-CO_2 in this experiment, 50 mL/min, was nearly two times greater than that of water in the MIU, 30 mL/min, the crack extension of 3.33 m vertically and 2 m horizontally was still quite greater than that of water. This difference could be attributed to the effect of expanding gaseous pressure with the phase change of CO_2 from SC to a gas, as well as lower viscosity of the CO_2 gas than that of liquid water.
3. After 1 min 15 s from BD, AE hypocenters started to distribute along the direction almost perpendicular to that of the initial crack induced by HF from the position of 0.6 m from the HF hole. Because no pressure acted in the pressurizing section of the HF hole in the term, a pre-existing crack most likely existed in a position along that direction. If so, this indicates that CO_2 can easily intrude and enhance AE occurrence along a pre-existing crack without pressure.
4. From the examination of the focal mechanisms by using P wave first-motion polarities of the AE events, we found that type T (tensile-dominated) events occurred near the pressurizing section of the HF hole immediately after BD. Findings from laboratory experiments by many researchers, as well as our similar recently conducted field experiment, suggest that new crack propagation in intact rock is most likely induced by tensile fracturing. The fact that type T events were induced immediately after BD is consistent with the results from previous experiments and the conventional elastic theory, which state that tensile fracture initiates HF.
5. After type T events were recorded, many type S (shear-dominant) events were recorded with type C (compression-dominant) events. When cracks extended from intact rock around the pressurizing section of the HF hole into inhomogeneous rock having various weak discontinuities including pre-existing cracks, many type S events were likely induced with new crack extension or slippage on planes of pre-existing cracks. In addition to the mechanism, it is likely that pore pressure increased with HF and its increase also enhanced shear events.
6. Many type C events were recorded with type S events in this experiment, although type C events were never observed in our similar HF experiment using water in the MIU. Thus, type C events are probably a distinct feature associated with CO_2 injection. Compressive events have been observed in volcanic regions and a geothermal reservoir, and they were attributed to crack closure due to degassing from magma in volcanic regions and the removal of steam in a geothermal reservoir. Thus,

the type C events observed in our present experiment were most likely induced by crack closure due to the degassing of injected CO_2. Even if CO_2 injection induced many AE events, compressive events (like the type C event) out of them unlikely trigger natural earthquakes because they never created new cracks.

Acknowledgements

This work was financially supported by the Japan Society for the Promotion of Science Grants-in-Aid for Scientific Research (A), Grant Numbers 25249131. We appreciate Mr. Shuhei Inui and Mr. Hiroto Yamashita, both Master students of Kyoto University, for their supports in the field monitoring and valuable comments on the monitoring results while we conducted this experiment.

Declaration of interests

The authors declare that they have no known competing financial interests or personal relationships that could have appeared to influence the work reported in this paper.

References

1. Xie H, Li X, Fang Z, Wang Y, Li Q, Shi L, Bai B, Wei N, Hou Z. Carbon geological utilization and storage in China: current status and perspectives. Acta Geotechnica. 2014; 9: 7–27.
2. Brown DW. A hot dry rock geothermal energy concept utilizing supercritical CO_2 instead of water, paper presented at 25th Workshop on Geothermal Reservoir Engineering. 2000; Stanford Univ., Stanford, Calif.
3. Pruess K. Enhanced geothermal systems (EGS) using CO_2 as working fluid—A novel approach for generating renewable energy with simultaneous sequestration of carbon, Geothermics. 2006; 35: 351–367.
4. Kalantari-Dahaghi A. Numerical simulation and modeling of enhanced gas recovery and CO_2 sequestration in shale gas reservoirs: A feasibility study, paper presented at International Conference on CO_2 Capture, Storage, and Utilization. 2010; Soc. of Pet. Eng., New Orleans, La.
5. Liu F, Ellett K, Xiao Y, Rupp JA. Assessing the feasibility of CO_2 storage in the New Albany Shale (Devonian- Mississippian) with potential enhanced gas recovery using reservoir simulation, Int J Greenh. Gas Control. 2013; 17: 111–126.
6. Middleton RS, Carey JW, Currier R.P, Hyman JD, Kang Q, Karra S, Jiménez-Martínez J, Porter ML, Viswanathan HS. Shale gas and non-aqueous fracturing

fluids: Opportunities and challenges for supercritical CO_2, Appl Energy. 2015; 147: 500–509.

7. Godec M, Koperna G, Petrusak R, Oudinot A. Potential for enhanced gas recovery and CO_2 storage in the Marcellus shale in the Eastern United States, Int J Coal Geol. 2013; 118: 95–104.
8. Nuttall BC, Drahovzal JA, Eble CF, Bustin RM. CO_2 Sequestration in Gas Shales of Kentucky, poster no. 106 at the 5th Annual Conference on Carbon Capture and Sequestration. 2006; Alexandria, VA, USA.
9. Ishida T, Aoyagi K, Niwa T, Chen Y, Murata S, Chen Q, Y. Nakayama Y. Acoustic emission monitoring of hydraulic fracturing laboratory experiment with supercritical and liquid CO_2. Gephys Res Lett 2012; 39: L16309.
10. Ishida T, Chen Y, Bennour Z, Yamashita H, Inui S, Nagaya Y, Naoi M, Chen Q, Nakayama Y, Nagano Y. Features of CO_2 fracturing deduced from acoustic emission and microscopy in laboratory experiments, J Geophys Res Solid Earth. 2016; 121(11): 8080–8098. doi:10.1002/2016JB013365.
11. Ishida T, Desaki S, Yamashita H, Inui S, Naoi M, Fujii H, Katayama T. Injection of supercritical carbon dioxide into granitic rock and its acoustic emission monitoring, Procedia Engineering. 2017; 191: 476-482. (Proc. of Eurock 2017, Paper No. 106, Ostrava, Czech Republic, 2017.) doi: 10.1016/j.proeng.2017.05.206
12. Ishida T, Desaki S, Kishimoto Y, Naoi M, Fujii H. Implosive acoustic emissions induced by injection of supercritical carbon dioxide into a hot granitic rock mass, Geomechanics and Geodynamics of Rock Masses. 2018; 1369–1374, Taylor & Francis Group, London. (Proc. of the International European Rock Mechanics Symposium, EUROCK 2018, Saint Petersburg, Russia, 22-26 May 2018), ISBN 978-1-138-61645-5)
13. Ishida T, Sasaki S. Numerical simulation to examine accuracy of AE source location and its applications to in-situ rock monitoring, J Acoust Emission. 2011; 29: 260–272.
14. Ishida T, Fujito W, Yamashita H, Naoi M, Fuji H, Suzuki K, Matsui H. Crack expansion and fracturing mode of hydraulic refracturing from acoustic emission monitoring in a small-scale field experiment, Rock Mech Rock Eng. 2019; 52(2): 543-553. doi: 10.1007/s00603-018-1697-5
15. Hubbert MK, Willis DG. Mechanics of hydraulic fracturing, Trans Am Inst Min Metall Petrol Engrs. 1957; 210: 153-168.
16. Zoback MD, Rummel F, Jung R, Raleigh CB. Laboratory hydraulic fracturing experiments in intact and pre-fractured rock, Int J Rock Mech Min Sci. & Geomech

Abstr. 1977; 14: 49-58.

17. Haimson BC. The hydrofracturing stress measuring method and recent field results, Int J Rock Mech Min Sci & Geomech Abstr. 1978; 15: 167-178.

18. Schmitt DR, Zoback MD. Infiltration effects in the tensile rupture of thin walled cylinders of glass and granite: Implications for the hydraulic fracturing breakdown equation, Int J Rock Mech Min Sci & Geomech Abstr. 1993; 30: 289-303.

19. Talebi S, Cornet FH. Analysis of the microseismicity induced by a fluid injection in a granitic rock mass, Geophys Res Lett. 1987; 14: 227–230.

20. Cornet FH. Fracture processes induced by forced fluid percolation, Volcanic Seismology, IAVCEI Proceedings in Volcanology, vol 3, edited by Gasparini P, Scarpa R, Aki K, Springer Verlag, 1992; 407–431.

21. Horálek, J., Jechumtálová Z, Dorbath L, Šílený J. Source mechanisms of micro-earthquakes induced in a fluid injection experiment at the HDR site Soultz-sous-Forêts (Alsace) in 2003 and their temporal and spatial variations, Geophys J Int. 2010; 181: 1547-1565.

22. Maxwell SC, Cipolla C. What does microseismicity tell us about hydraulic fracturing? SPE Annual Technical Conference and Exhibition, Denver, Colorado, USA, 2011; SPE 146932.

23. Ross A, Foulger GR, Julian BR. Non-double-couple mechanisms at The Geysers geothermal area, California, Geophys Res Lett. 1996; 23: 877–880.

24. Vavryčuk V. Non-double-couple earthquakes of 1997 January in West Bohemia, Czech Republic: evidence of tensile faulting, Geophys J Int. 2002; 149: 364-373.

25. Šílený J, Hill DP, Eisner L, Cornet FH. Non-double-couple mechanisms of microearthquakes induced by hydraulic fracturing, J Geophys Res. 2009; 114: B08307. doi:10.1029/2008JB005987.

26. Julian BR, Foulger GR, Monastero FC, Bjornstad S. Imaging hydraulic fracturing in a geothermal reservoir, Geophys Res Lett. 2010; 37: L07305. doi:10.1029/2009GL040933.

27. Sasaki S, Matsunaga I, Kobayashi H, Ishida T. Development of a fracture evaluation technique for HDR geothermal energy extraction --- Mechanism of hydraulic fracturing inferred from acoustic emission ---. Central Research Institute of Electric Power Industry, Abiko Research Laboratory Report, 1988; U88034 (in Japanese with English abstract and figure captions)

28. Dale TN. The commercial granites of New England(I), U.S. Geological Survey Bull. 1923; 738: 1-97.

29. Sano S, Kudo Y, Mizuta Y. Experimental determination of elastic constants of

Oshima granite, Barre granite, and Chelmsford granite, J Geophys Res. 1992; 97(B3): 3367-3379.

30. Ishida T. Acoustic emission monitoring of hydraulic fracturing in laboratory and field, Construction and Building Materials. 2001; 15: 283–295. doi: 10.1016/S0950-0618(00)00077-5.

31. Yamamoto K, Naoi M, Chen Y, Nishihara K, Yano S, Kawakata H, Akai T, Kurosawa I, Ishida T. Moment tensor analysis of acoustic emissions induced by laboratory-based hydraulic fracturing in granite, Geophys J Int. 2019; 216(3): 1507–1516. doi: 10.1093/gji/ggy493.

32. Rodriguez IV, Stanchits S, Burghardt J. Data-driven, in situ, relative sensor calibration based on waveform fitting moment tensor inversion. Rock Mech Rock Eng. 2017; 50: 891–911. doi: 10.1007/s00603-016-1144-4

33. Hill DP. A model for earthquake swarms, J Geophys Res. 1977; 82: 1347-1352

34. Kao CS, Carvalho FCS, Labuz JF. Micromechanisms of fracture from acoustic emission, Int J Rock Mech Min Sci. 2011; 48: 666–673.

35. Shimizu H, Ueki S, Koyama J. A tensile-shear crack model for the mechanism of volcanic earthquakes, Tectonophysics. 1987; 144, 287-300.

36. Foulger GR, Long RE, Einarsson P, Bjornsson A. Implosive earthquakes at the active accretionary plate boundary in northern Ice land, Nature. 1989; 337: 640-642, doi:10.1038/337640a0.

37. Martínez-Garzón P, Kwiatek G, Bohnhoff M, Dresen G. Volumetric components in the earthquake source related to fluid injection and stress state, Gephys Res Lett. 2017; 44: 800‑809. doi:10.1002/2016GL071963.

38. Bonhoff M, Zoback MD. Oscillation of fluid-filled cracks triggered by degassing of CO_2 due to leakage along wellbores, J Geophys Res. 2010; 115: B11305, doi:10.1029/2010JB000848.

39. Warjito, Mochizuki O, Ishikawa H. Breakup of a single babble and its sound, Nagare. 2002; 21: 165-172 (in Japanese with English abstract)

40. Kolaini AR. Effects of salt on babble acoustic radiation in water, Journal of the Acoustical Society of America. 1999; 105(4): 2181-2186.

Figure Captions

Figure 1 Site and experimental setup. (a) Layout of test site. [11, 12] (b) Arrangement of acoustic emission (AE) sensors surrounding a pressurized section under the test site. The inset shows a dimensioned diagram of packer used to seal the pressurized section.

Figure 2 Injection system for SC-CO_2.[11, 12]

Figure 3 Phase diagram of CO_2.[11, 12]

Figure 4 Temporal changes of fluid pressure, temperature, AE rate, and flow rate. Thick line segments on the fine line in Figure 4b indicate terms missing AE data.[11, 12]

Figure 5 Projections of AE hypocenters onto horizontal plane, *XY*, and two vertical planes, *YZ*, and *ZX*, where *X* axis is parallel to the direction from the hole AE1 to AE2 and that from AE4 to AE3, *Y* axis is perpendicular to *X* axis and *Z* axis is the vertical. The origin is placed at the center of HF hole on the horizontal plane, *XY*. The bars and the open rectangles on the *YZ* and *ZX* planes correspond to HF and AE holes and AE sensors, respectively. The broken lines on them indicate pressurizing section from 7.24 to 7.40 m. Note that +X direction is from right to left.[11, 12]

Figure 6 AE hypocenter distributions on horizontal *XY* plane, for period from 0 to 1 min 15 s in comparison with those from 1 min 15 s to 30 min 0 s.[11, 12]

Figure 7 Photo of a core of 36 mm diameter pilot hole drilled to make pressurize section before HF and a hollow core recovered by 86 mm diameter overcoring around pressurizing section after HF.

Figure 8 Cracks observed on wall of HF hole with a borehole camera after HF. CO_2 injected in section from 7.24 to 7.40 m most likely induced cracks traced with the black lines. Yellow thick lines indicate open cracks of aperture within 0.5 mm, whereas yellow broken lines indicate closed adherent cracks.

Figure 9 Compressive ratio *R* (%) of P wave first-motion polarity of AE. In the present study, we labelled AE with $100 \geq R \geq 80$, $80 > R > 20$ and $20 \geq R \geq 0$ as tensile-dominant (type T: red stars), shear-dominant (type S: blue circles) and compression-dominant (type C: green circles), respectively.[12]

Figure 10 *X*, *Y*, and *Z* coordinates of AE hypocenters along with elapsed times for 30 min after BD, corresponding to those of Figure 9. Red stars, open blue circles and closed green circles indicate the same AE types as those in Figure 9. A band of broken lines on the Z coordinate indicates the span of pressurizing section in the pilot hole.

Figure 11 Distributions of AE hypocenters projected on horizontal plane, *XY*. (a) From 0 s to 1 min 15 s. (b) From 1 min 15 s to 30 min 0 s. Figures 11a and 11b plot only 161 AE in total out of the 1249 well-located AE hypocenters plotted in Figures 6 and 7. The 161 AE correspond to those shown in Figures 9 and 10.

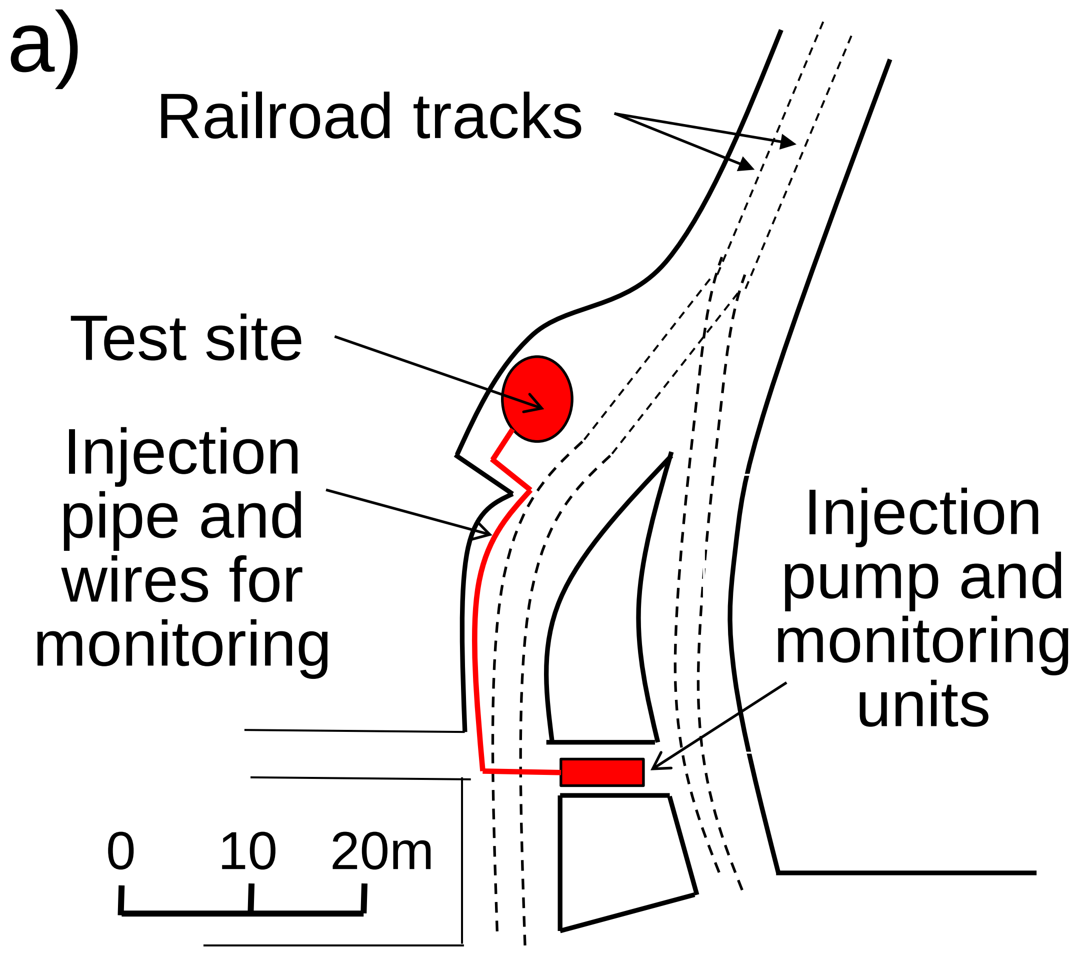
a)
Railroad tracks
Test site
Injection pipe and wires for monitoring
Injection pump and monitoring units
0 10 20m

Figure 1a

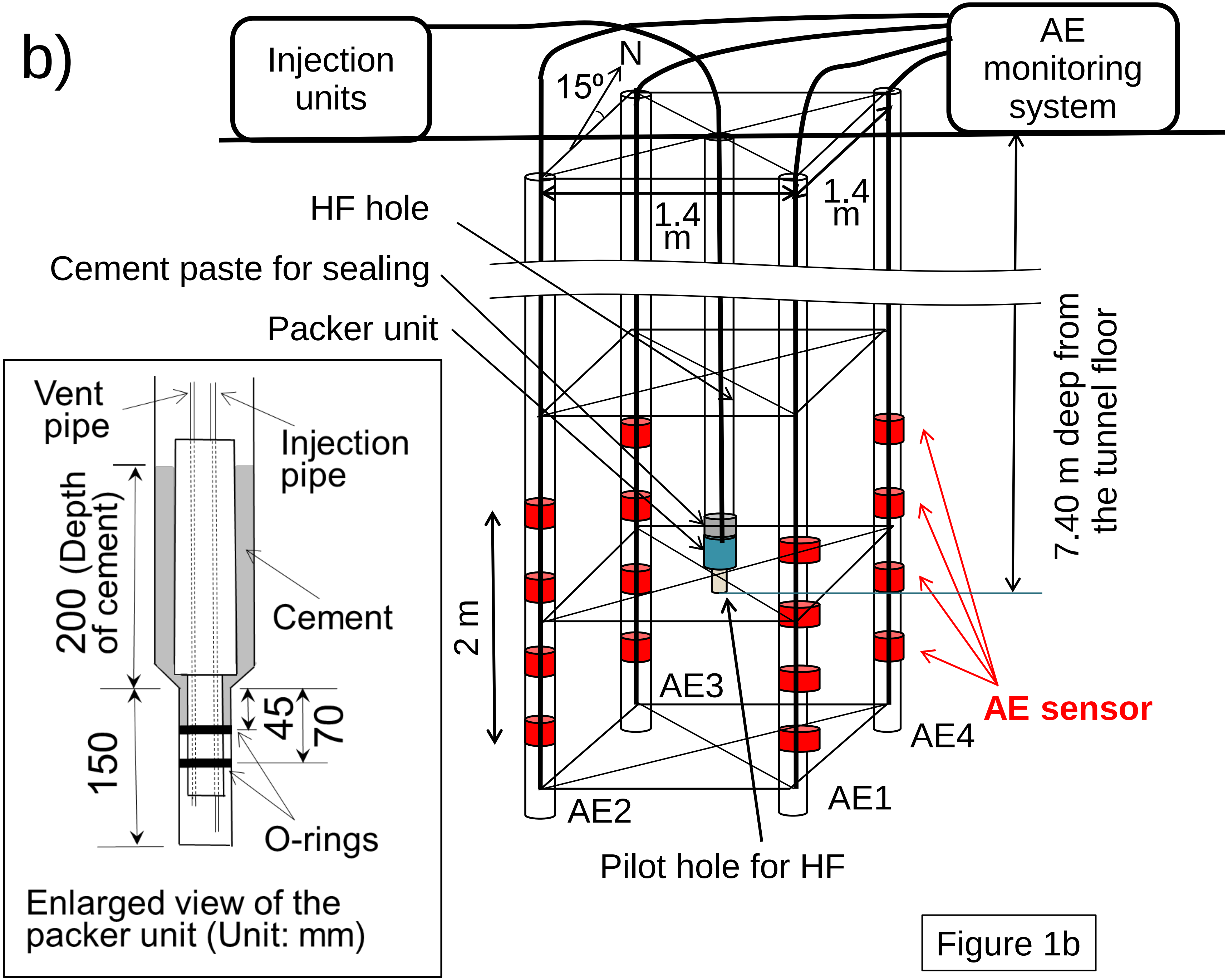

b)
Injection units
AE monitoring system
N
15º
1.4 m
1.4 m
HF hole
Cement paste for sealing
Packer unit
7.40 m deep from the tunnel floor
2 m
AE3
AE4
AE2
AE1
AE sensor
Pilot hole for HF
Vent pipe
Injection pipe
200 (Depth of cement)
Cement
150
45
70
O-rings
Enlarged view of the packer unit (Unit: mm)

Figure 1b

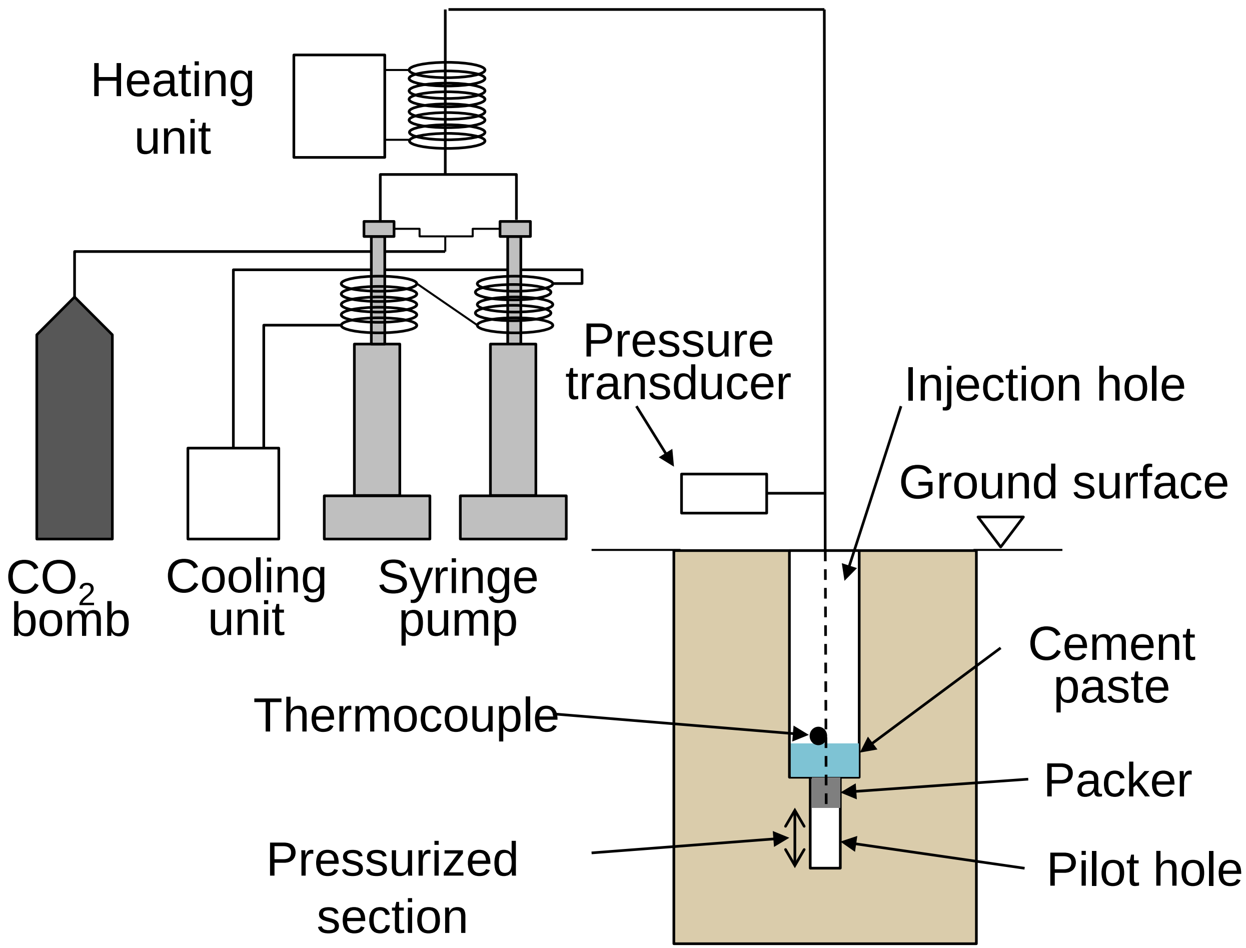
Heating
unit
Pressure
transducer
Injection hole
Ground surface
CO_2
bomb
Cooling
unit
Syringe
pump
Cement
paste
Thermocouple
Packer
Pressurized
section
Pilot hole

Figure 2

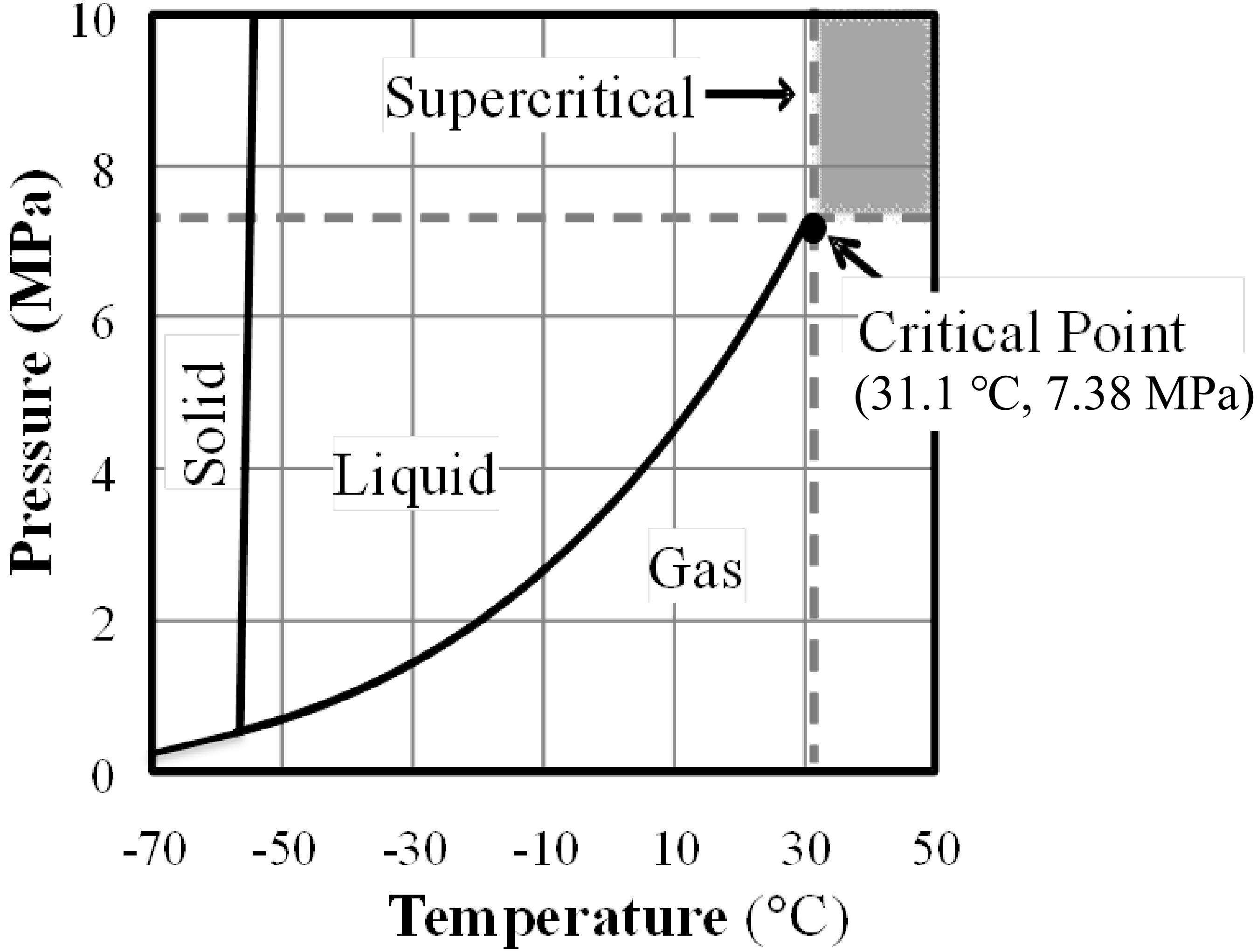
Supercritical
Critical Point
(31.1 °C, 7.38 MPa)
Solid
Liquid
Gas
Pressure (MPa)
10
8
6
4
2
0
-70
-50
-30
-10
10
30
50
Temperature (°C)

Figure 3

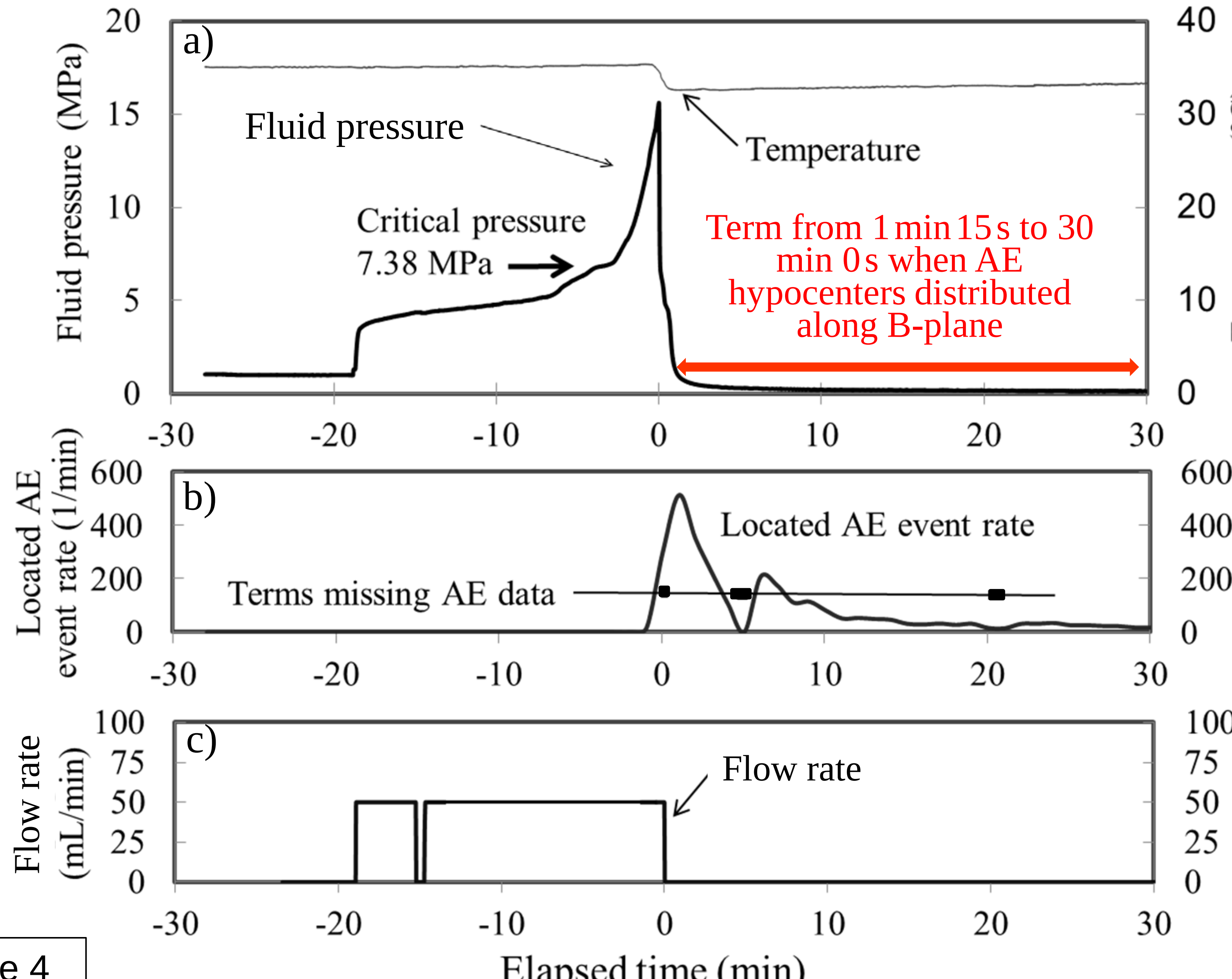

a)
Fluid pressure
Temperature
Critical pressure
7.38 MPa
Term from 1 min 15 s to 30 min 0 s when AE hypocenters distributed along B-plane
Fluid pressure (MPa)
Temperature (°C)
b)
Located AE event rate
Terms missing AE data
Located AE event rate (1/min)
c)
Flow rate
Flow rate (mL/min)
Elapsed time (min)

Figure 4

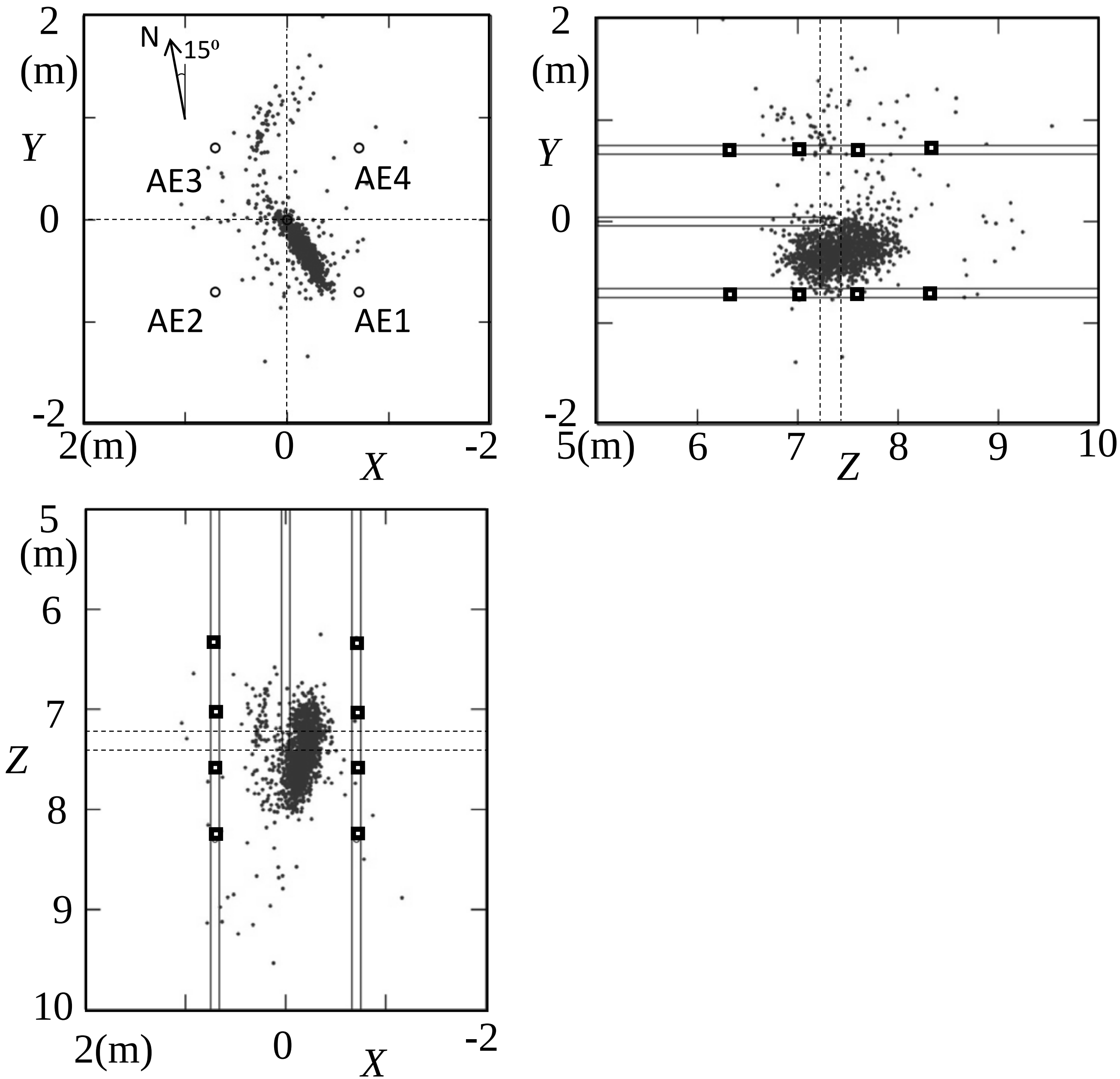

2
(m)
N
15º
Y
AE3
AE4
0
AE2
AE1
-2
2(m)
0
X
-2
2
(m)
Y
0
-2
5(m)
6
7
Z
8
9
10
5
(m)
6
7
Z
8
9
10
2(m)
0
X
-2

Figure 5

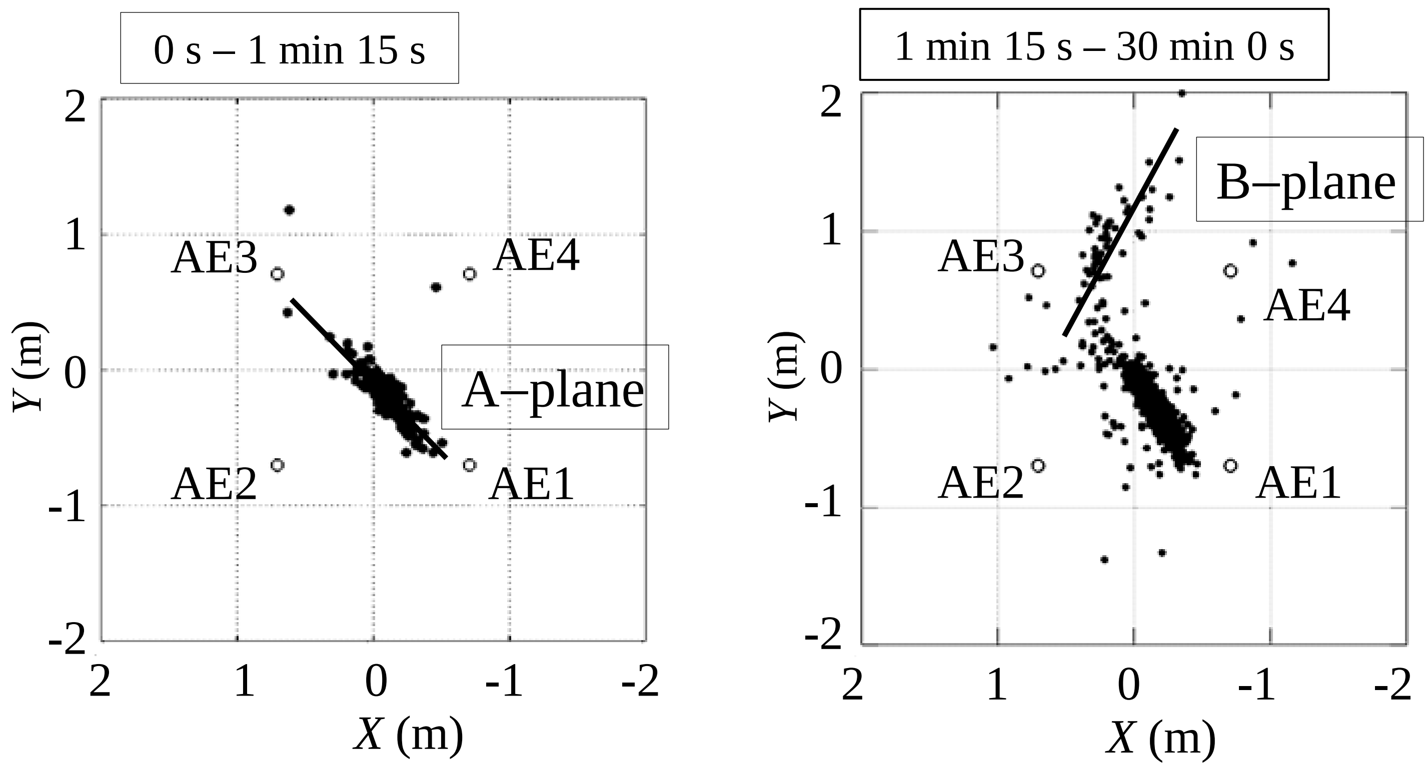
0 s – 1 min 15 s
A–plane
AE1
AE2
AE3
AE4
Y (m)
X (m)
2
1
0
-1
-2
1 min 15 s – 30 min 0 s
B–plane
AE1
AE2
AE3
AE4
Y (m)
X (m)

Figure 6

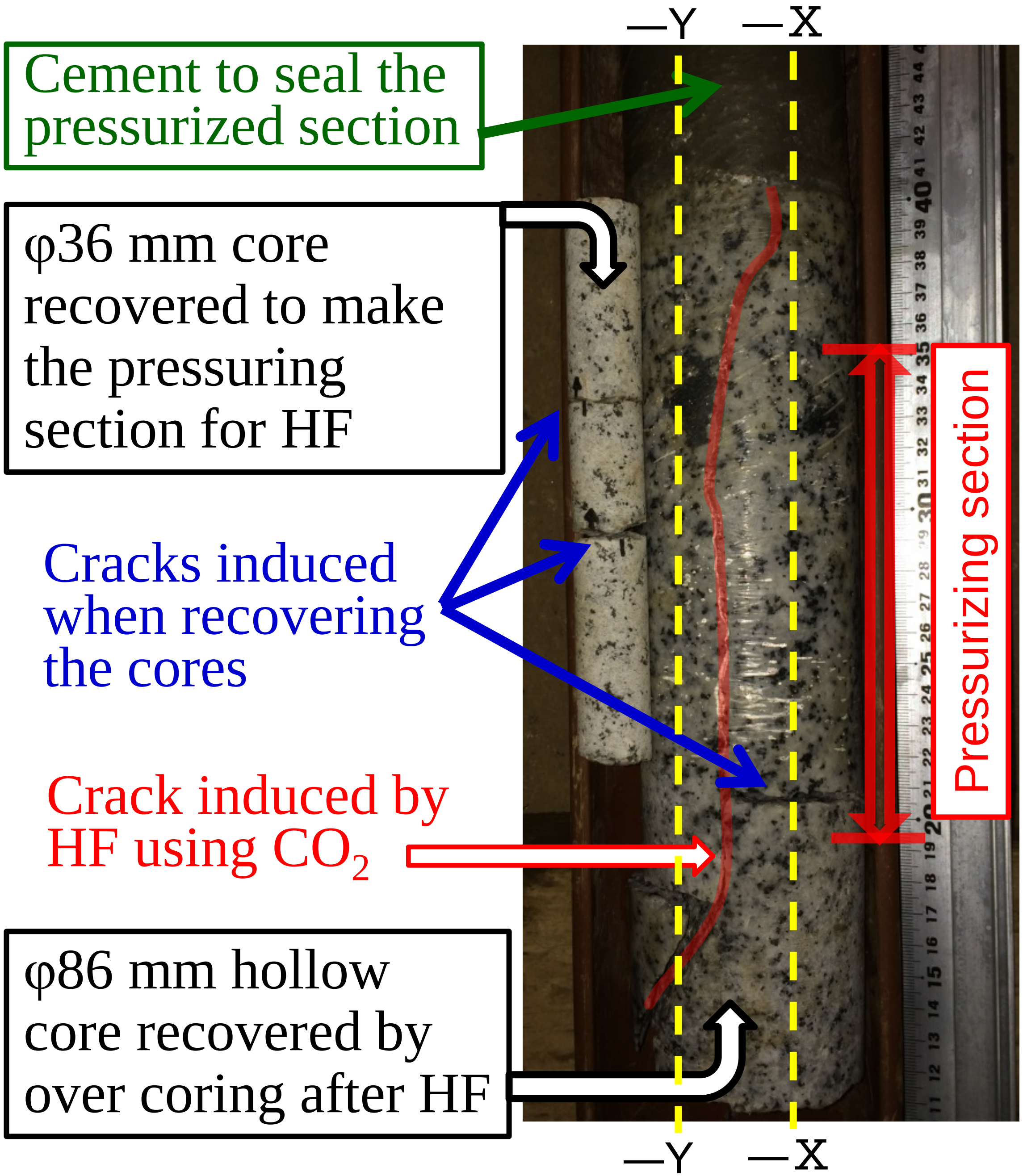

—Y
—X
Cement to seal the pressurized section
φ36 mm core recovered to make the pressuring section for HF
Cracks induced when recovering the cores
Crack induced by HF using CO_2
φ86 mm hollow core recovered by over coring after HF
Pressurizing section
—Y
—X

Figure 7

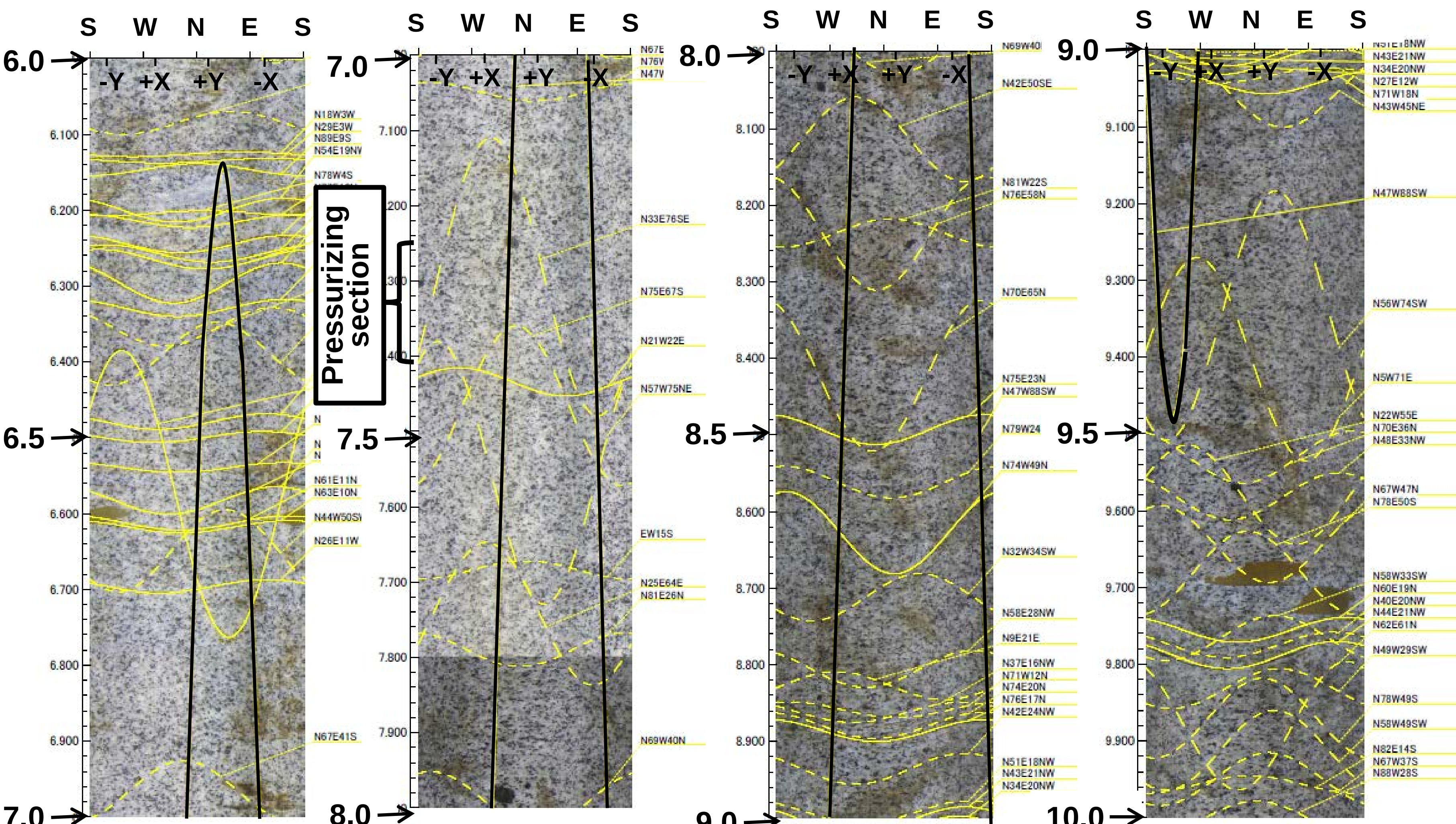

Figure 8

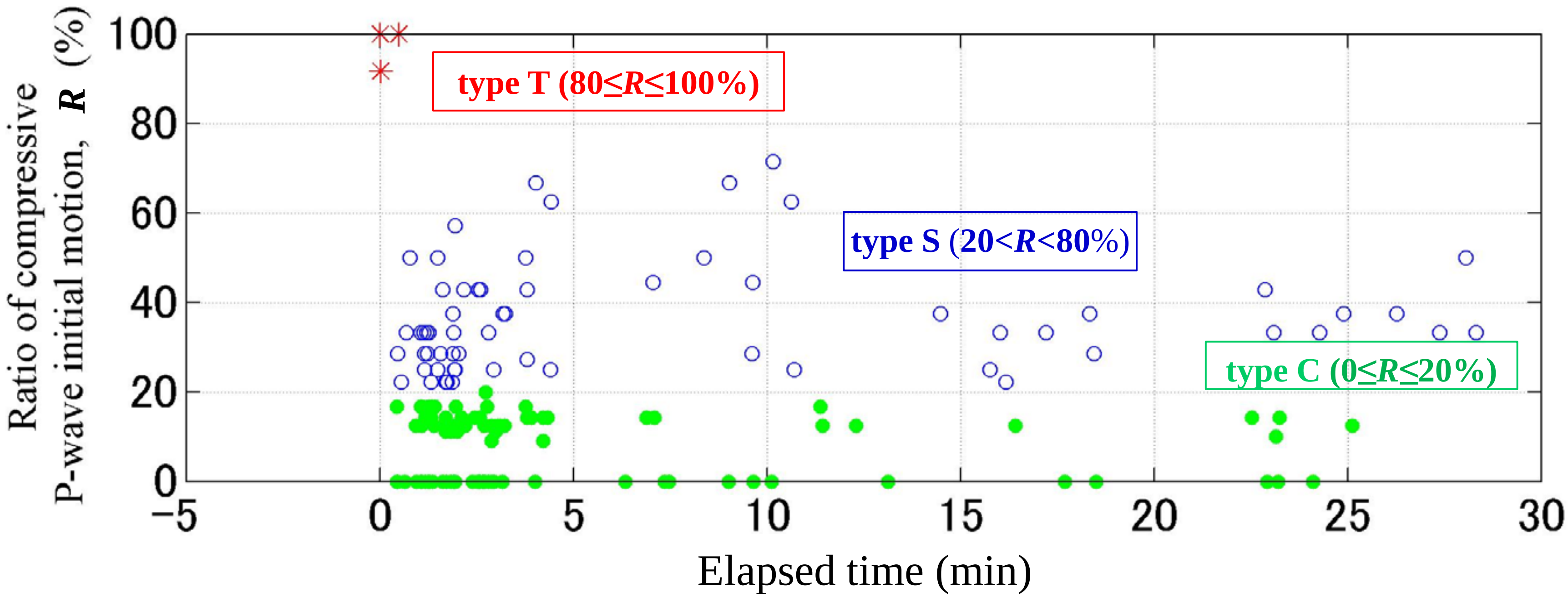

Ratio of compressive P-wave initial motion, R (%)
type T (80≤R≤100%)
type S (20<R<80%)
type C (0≤R≤20%)
100
80
60
40
20
0
−5
0
5
10
15
20
25
30
Elapsed time (min)

Figure 9

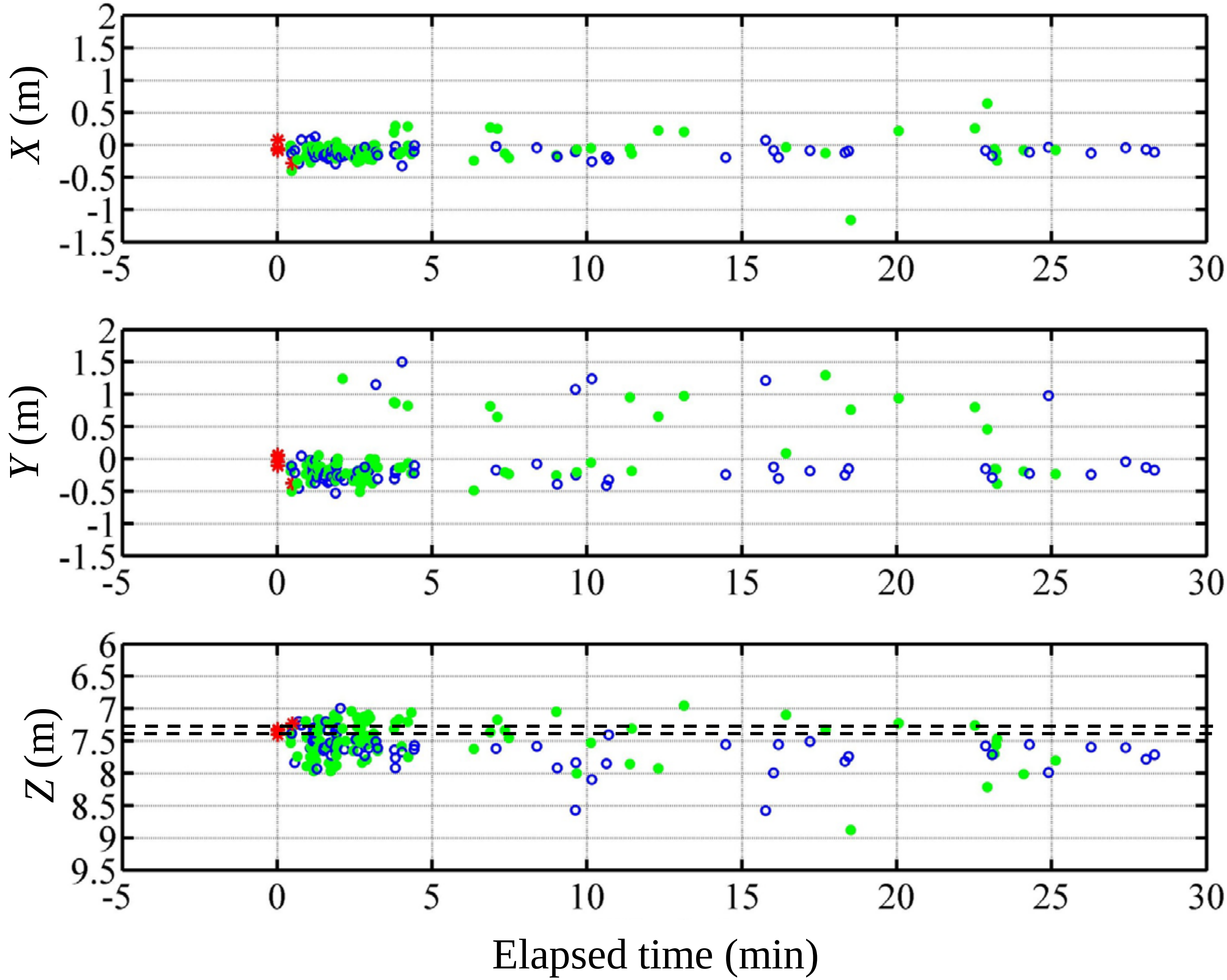
X (m)
2
1.5
1
0.5
0
-0.5
-1
-1.5
-5
0
5
10
15
20
25
30
Y (m)
2
1.5
1
0.5
0
-0.5
-1
-1.5
-5
0
5
10
15
20
25
30
Z (m)
6
6.5
7
7.5
8
8.5
9
9.5
-5
0
5
10
15
20
25
30
Elapsed time (min)

Figure 10

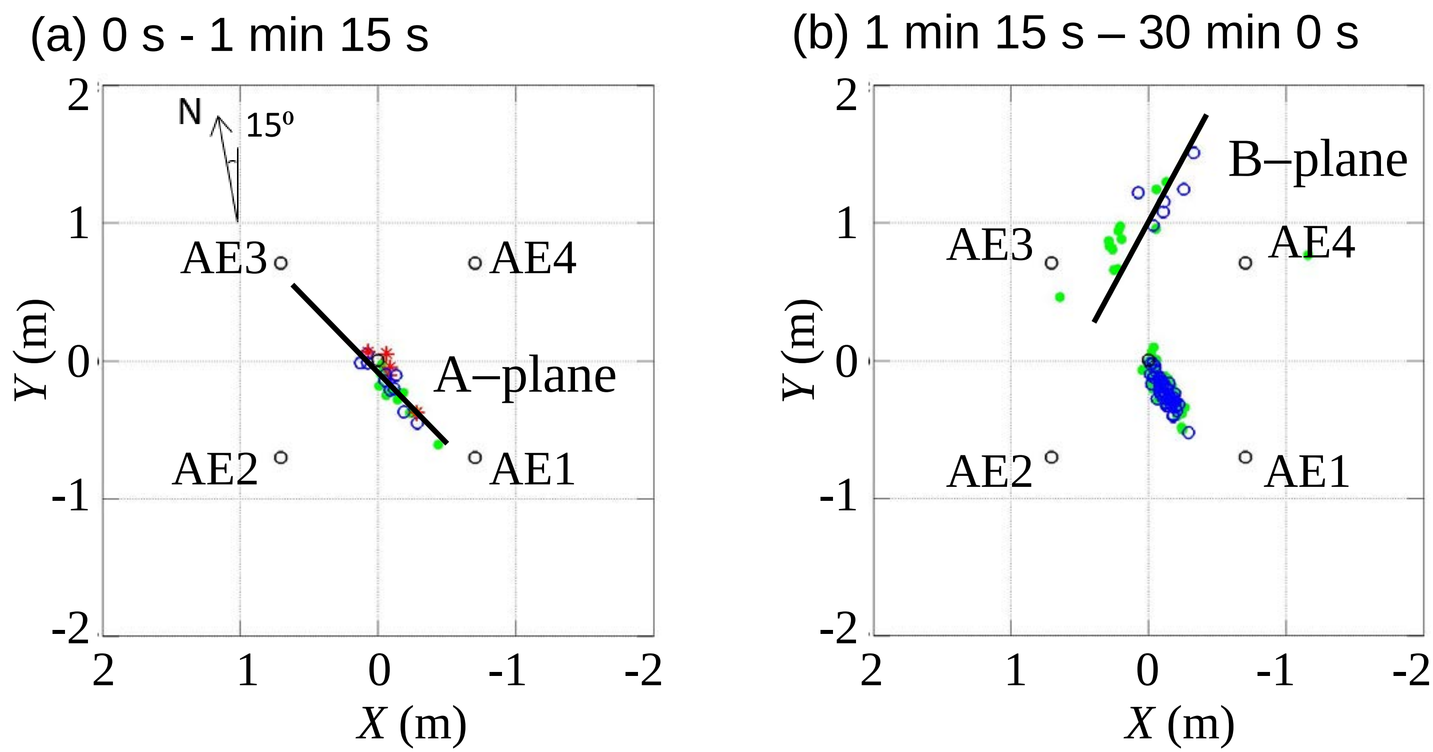
(a) 0 s - 1 min 15 s
(b) 1 min 15 s – 30 min 0 s
N
15º
AE1
AE2
AE3
AE4
A–plane
B–plane
Y (m)
X (m)
2
1
0
-1
-2

Figure 11